UCLA
COMPUTATIONAL AND APPLIED MATHEMATICS

Behavior of a Sand Ridge Model

Juan Mario Restrepo

May 1997

CAM Report 97-22

Department of Mathematics
University of California, Los Angeles
Los Angeles, CA. 90095-1555

BEHAVIOR OF A SAND RIDGE MODEL

JUAN MARIO RESTREPO

Mathematics Department
University of California, Los Angeles
Los Angeles, CA 90095

ABSTRACT. A model for the formation and evolution of longshore sand ridges in waters deeper than the shoaling region suggests that a possible but by no means exclusive agent for the formation of these bars are weakly nonlinear dispersive long waves. The model describes how these water waves, which are represented by wave packets, and a sandy bottom topography, conspire to produce sand ridges. This study examines the behavior of the model, and investigates how specific morphological features of the sand ridges depend on the water waves' characteristics.

1. INTRODUCTION

A model for the formation and evolution of three-dimensional longshore sand ridges on the continental shelf was proposed in [3], [10], [14], and [13]. It identifies weakly nonlinear, dispersive shallow-water waves as the agents of formation of these structures. Assuming the fluid has constant density, is incompressible and irrotational, and that dissipative processes can be ignored, these waves are governed by the dimensionless regularized Boussinesq system

$$\begin{aligned} \eta_t + \nabla \cdot [(h + \alpha\eta)\mathbf{u}] - \frac{1}{3}\beta^2 \nabla \cdot [\nabla(h^2 \eta_t)] &= 0 \\ \mathbf{u}_t + \alpha(\mathbf{u} \cdot \nabla)\mathbf{u} + \nabla\eta &= 0, \end{aligned} \tag{1}$$

where $\eta(x, y, t)$ and $\mathbf{u}(x, y, t)$ connote the amplitude and transverse velocity of the water waves, respectively. The shoreward coordinate is denoted by x and the spanwise coordinate by y. Time is denoted by t. The parameters $\alpha \ll 1$ and $\beta^2 \ll 1$ are the degree of nonlinearity and dispersion in the waves, respectively. Eq. (1) was derived under the assumption that $O(\alpha) \sim O(\beta^2)$, however, it has been shown in [6] that models of this type are quite robust and capable of modeling waves in the Stokes régime $\alpha/\beta^2 = O(10 - 50)$, which is an estimate of the oceanic situation in which the sand ridges are known to occur.

Key words and phrases. sandbars, sand ridges, nonlinear dispersive waves.

Work supported by an appointment to the Distinguished Postdoctoral Research Program sponsored by the U.S. Department of Energy, Office of University and Science Education Programs, and administered by the Oak Ridge Institute for Science and Education. Mr. Andrés Martínez Tejada's help in generating some of the figures is much appreciated.

The vertical coordinate, denoted by z, is zero at the level corresponding to the quiescent ocean. The ocean surface corresponds to $z = \eta$ and the bottom to $z = -h$. The bottom topography evolves in time, with typical scale T, which is much longer than the time t tracking the progress of the hydrodynamics. The bottom topography is described by $h = 1 + f(X, y, T)$, where $f = O(1)$ and is assumed smooth and gently changing in $X = \alpha x$ and y.

Although the model for the water waves is the Boussinesq system, a wave packet representation for the solutions of Eq. (1) is an approximation with some merit, since it captures some of the essential characteristics of the water wave model, easily providing valuable insight on some of the qualitative features of the sand ridge evolution model. The wave packet representation is valid provided multiple scales are clearly defined and the spectra of the water waves is amenable to a somewhat arbitrary separation into weakly interacting wave packets. For presentation purposes, two interacting wave packets will be considered. Hence, the dynamics of the surface waves are simplified by assuming

$$u(x, X, y, t) = \sum_{j=1}^{2} [a_j(X, y) + O(\alpha)] e^{i(k_j x - \omega_j t)} + c.c., \tag{2}$$

a crude but still very useful ansatz. The symbol c.c. stands for complex conjugate of the expression immediately preceding its appearance. The a's are the complex incident wave packet amplitudes. These packets are assumed to have significant spectral support in $\Delta k_j \ll k_j$, where k_j is the wavenumber of the j-th carrier wave. The reality of the physical variables implies that $a_{-j} = a_j^\star$. For simplicity, the reflected component of the water waves has been neglected. Furthermore, it is assumed that the waves travel almost perpendicular to the shore, which is in the direction in which x increases, and have weak spanwise y dependence. If their spanwise dependence is weak enough, the parabolic approximation holds [10], thus,

$$\begin{aligned} y &\leftarrow \alpha^{1/2} y, \\ \hat{y} \cdot \mathbf{u} &\leftarrow \alpha^{-1/2} \hat{y} \cdot \mathbf{u}. \end{aligned}$$

Since $u_t + \eta_x = 0$ holds at lowest order in the momentum balance, an expression for the surface amplitude η is readily available:

$$\eta = \sum_{j=1}^{2} \frac{\omega_j}{k_j} [a_j(X, y) + O(\alpha)] e^{i(k_j x - \omega_j t)} + c.c. \tag{3}$$

A plane-wave solution of the form given by Eqs. (2) and (3) is valid, provided that the relation

$$\omega_j^2 - k_j^2 \left(1 + \frac{\beta^2 k_j^2}{3} \right)^{-1} = 0 \tag{4}$$

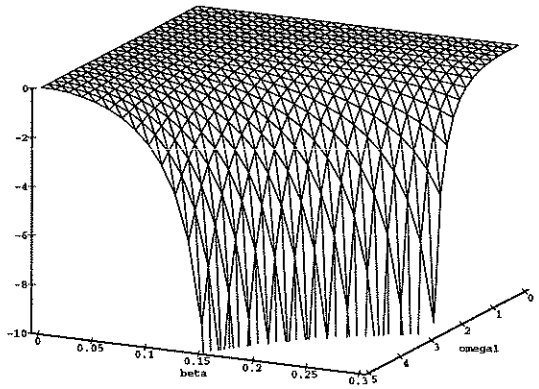

FIGURE 1. Detuning parameter $\tilde{\delta}$ dependence on the fundamental frequency ω_1 and the dispersion parameter β for the water wave problem.

holds, between the carrier frequency ω_j, and the carrier wavenumber k_j. Eq. (4) is the dispersion relation for the j-th carrier, the positive root k_j corresponding to the shoreward-directed wave. In this way, $\omega_2 = 2\omega_1$, and $k_2 = 2k_1 - \tilde{\delta}$, where $\tilde{\delta} \leq 0$. A plot of the detuning parameter $\tilde{\delta}$ as a function of the fundamental frequency ω_1 and β for the water wave problem, is shown in Figure 1.

A compatibility condition yields the equations for the spatial evolution of the surface wave amplitudes, namely,

$$\begin{aligned} a_{1X} - iK_1 a_{1yy} + iK_3 f(X,y)a_1 + iK_5 e^{-i\delta X} a_1^\star a_2 &= 0 \\ a_{2X} - iK_2 a_{2yy} + iK_4 f(X,y)a_2 + iK_6 e^{+i\delta X} a_1^2 &= 0 \\ a_1(X=0,y) &= \mathcal{A}_1(y,\tau) \\ a_2(X=0,y) &= \mathcal{A}_2(y,\tau), \end{aligned} \tag{5}$$

where $\delta = \tilde{\delta}/\alpha$ will be known as the detuning parameter and is $O(1)$. To complete the problem boundary conditions must be specified on $y = 0$ and $y = Y$. These boundary conditions are chosen in such a way that they do not introduce unwanted structure in the solutions (see [12] for details). The K's are real constant coefficients described in the Appendix section. The data $\mathcal{A}_i$, where $i = 1, 2$, are given by the spectra of the incoming wave field measured at the line $X = 0$. This spectra will change in time, with time scale τ, but at a rate much slower than the evolution times of the water waves themselves. The time scale τ is determined by changes in the meteorological conditions which significanty affect the infra-gravity oceanic spectra and is smaller or comparable to the time scale T. In this study we will not have occasion to explore the effects of time-dependent spectral data hence the $\mathcal{A}_i's$ will be subsequently assumed constant.

The water waves provide the driving agent for the motion of the suspended sediment in the turbulent boundary layer hugging the bottom. Moreover, the water waves endow the velocity in the boundary layer with spatial structure which then influences the spatial deposition and scouring of a sedimentary bed. In this model the evolution of the bottom

topography is assumed to occur in time scales typical of $T \gg t$, time scales in which the boundary layer drift velocity has a significant effect in advecting sediment in the transerve directions X and y. The sediment concentration is governed by an advection-diffusion equation. Since the suspended sediment is concentrated almost entirely in the boundary layer and the water waves have very long wavelengths, as compared to the boundary layer thickness, it is easy to see that

$$\frac{\partial}{\partial z}\left(\rho + \nu_T \frac{\partial \rho}{\partial z}\right) = 0$$

provides an adequate approximation for the sediment concentration ρ, in the boundary layer of thickness δ_{bl}, for sediment with dimensionless settling velocity w_s, under the action of waves with typical orbital velocity U_∞. The turbulent eddy viscosity ν_T above has been made dimensionless by the factor $\delta_{bl} w_s U_\infty$, hence, it is an $O(1-10)$ quantity in the geophysical setting. Additional rules for the dynamics of the sand particles could also include intra-particle collision rules, and drag effects. However, aside from the assumption of the disparate time scales of evolution of the bottom and the hydrodynamics, the other feature that makes this model somewhat different from others is that it asserts that the structure of the sand ridges is almost entirely inherited from the structure in the drift velocity which is generated by the inviscid flow, rather than from details of the flow in the boundary layer. Hence, the dynamics of the sediment have little influence on the gross features of the bars. Moreover, although the boundary layer is turbulent, little qualitative difference is obtained by the adoption of different parameterizations of the eddy viscosity ν_T. This issue needs to be checked, and studies are under way to determine the veracity of this assertion. However, it seems to be a reasonable assumption, since sediment concentration in areas deeper than the shoaling region is quite low, and almost entirely concentrated in the boundary layer [4], and shearing forces due to these long waves are significant in a comparatively very thin boundary layer.

The evolution of the bottom topography, and to be approximately described by the mass transport equation

$$\frac{\partial f(X,y,T)}{\partial T} = \frac{K}{\rho_0}\left[\frac{\partial U}{\partial X} + \frac{\partial V}{\partial y}\right] \tag{6}$$

where K/ρ_0 is a positive constant of proportionality;

$$U(X,y) = \frac{1}{\delta_{bl}} \int_0^{\delta_{bl}} \rho(X,y,z')\mathcal{U}(X,y,z'))dz'$$

is the shoreward mass flux, and V is the spanwise component of the mass flux. In the above expression, the integration over the bottom-following vertical coordinate z' spans the thickness of the boundary layer δ_{bl}; ρ is the time-averaged suspended sediment concentration in the boundary layer, $\mathcal{U}$ is the X component of the Stokes drift [9] in the boundary layer generated by the surface water waves. Without forgetting the importance of the contribution of the sediment concentration distribution in the boundary layer on

the overall morphology of bedforms, in this presentation the issue of sediment dynamics will be ignored and it will be assumed hereon that the sediment concentration is uniform and constant throughout the boundary layer and equal to 1.

As mentioned above, the model assumes that the evolution of the bottom topography has characteristic time scales that are much longer than the time scales in which surface waves adjust to changes in the bottom topography: an incident wave field senses a bottom which is essentially fixed in time, from the moment it enters the purview of the model to the time it eventually leaves it. The bottom deforms slowly after the passage of many waves. The phase of these waves is fixed by the slowly-changing topography and meteorological forcing. These do not seem to change appreciably in time scales typical of the evolution of the waves. Owing to the widely discrepant time scales between the (fast) evolution of the water waves and the (slow) bottom topography, the coupled system, comprised of Eqs. (5) and (6), may be solved iteratively: given an initial bottom configuration $h(X, y, T_i) = \mathcal{F}(X, y)$, a solution to the water waves may be found using Eq. (5). The drift velocity is then calculated by solving for the Stokes drift in the boundary layer. The bottom is then updated using Eq. (6), and the wave packet equations are solved using the new bottom configuration. The whole procedure is repeated until some prescribed final time $T_f > T_i$, say. The input to the model is composed of an initial bottom configuration and the wave packet amplitudes at the line $X = 0$. The physical parameters set by field data are the fundamental frequency; the initial bottom configuration, and an estimate of the size of the parameters $\alpha \ll 1$ and $\beta \ll 1$, respectively.

This study is devoted to the analysis of the sand ridge model developed in [14] which has been summarized above. Of interest is to determine what aspects of the water waves determine features of the bar morphology and what types of sand ridges are steady wave/bottom configurations. In the process, we learn about the models' predictive capabilities and its weaknesses. Furthermore, we hope to discern how the more complex model, which uses a full Boussinesq equation for the water waves, and the sediment concentration equation, should behave under similar oceanic conditions.

The most interesting sand ridges are three-dimensional sedimentary structures. These would be solutions of the system of equations comprised of Eq. (5) and (6), which we will denote in this study as the "full model". However, as a first step, this study will be concerned with sand ridges with only height and shoreward dependence. The variant of the model with shoreward and depth dependence will be denoted the "reduced model". The reduced model will be considered in Section 2. Exploiting well-known results about the triad system represented by the wave packet equations, this paper will report on the steady-state bottom configurations for the reduced model in Section 3. The analysis will show that the behavior of the model falls into one of two dynamic regimes which can be classified by the value of a dimensionless parameter. Furthermore, it will show how dispersive and nonlinear effects in the water waves affect the shape, the interbar spacing, and the amplitude of the bars. Section 4 summarizes the findings of this study.

2. The Reduced Model

When the bottom only depends on X and T and the data at $X = 0$ is constant, the

solutions will not have spanwise dependency. In this case Eq. (5) reduces to

$$\begin{aligned} a_{1X} + iK_3 f(X) a_1 + iK_5 e^{-i\delta X} a_1^\star a_2 &= 0 \\ a_{2X} + iK_4 f(X) a_2 + iK_6 e^{+i\delta X} a_1^2 &= 0 \\ a_1(X=0,y) &= \mathcal{A}_1 \\ a_2(X=0,y) &= \mathcal{A}_2, \end{aligned} \tag{7}$$

where $\mathcal{A}_j$ are constants. Furthermore, the mass transport equation reduces to

$$\frac{\partial f(X,T)}{\partial T} = \frac{K}{\rho_0}\frac{\partial U}{\partial X}. \tag{8}$$

Eqs. (7) and (8) comprise the reduced model. In terms of the wave-packet amplitudes, the shoreward mass flux is

$$U = \sum_{j=1}^{2} C_j^2 |a_j|^2,$$

where $C_j = q_j[1 - \frac{1}{2}\beta^2 k_j^2 (1+f)^2]$, $j = 1, 2$, and q_j are boundary-layer dependent quantities (cf. [10]) that will be set to 1 in the remainder of this study.

Consider the wave-packet system when f is fixed in time. Eq. (7) is then familiar to the nonlinear optics and water wave community (cf. [2], [5], [16] and [1] and references contained therein). Some well-known results related to the wave packet system are reviewed in what follows. We will then proceed to use these results to elucidate the behavior of the reduced model.

Let $a_i = A_i(X) \exp \theta_i(X)$. Substituting into Eq. (7) yields

$$\begin{aligned} A_{1X} &= K_5 A_1 A_2 \sin\Omega \\ A_{2X} &= -K_6 A_1^2 \sin\Omega \\ \Omega_X &= -\delta - K_0 f(X) - \left[K_6 \frac{A_1^2}{A_2} - 2K_5 A_2\right] \cos\Omega, \end{aligned} \tag{9}$$

with $\Omega = 2\theta_1 - \theta_2 + \delta X$, and $K_0 = K_4 - 2K_3$. Replacing

$$\begin{aligned} M &= A_2 \sin\Omega \\ N &= A_2 \cos\Omega \\ P &= A_1^2, \end{aligned}$$

in Eq. (9) and performing some algebraic manipulations leads to a statement of conservation of energy

$$K_5(M^2 + N^2) + K_6 P = E_0, \tag{10}$$

as well as the equation

$$\frac{dM}{dN} = \frac{K_5(M^2+3N^2) - [\delta + K_0 f(X)]N - E_0}{([\delta + K_0 f(X)] - 2K_5 N)M}, \tag{11}$$

which may be used to investigate the structure of the phase plane of A_2. The dynamics of A_1 follow immediately from the conservation of the energy constraint. Let $\Delta(X) \equiv \delta + K_0 f(X)$, be the augmented detuning parameter, so that Eq. (11) may be written as

$$\frac{dM}{dN} = \frac{K_5(M^2+3N^2) - \Delta(X)N - E_0}{(\Delta(X) - 2K_5 N)M}. \tag{12}$$

When $\Delta = \delta$ the gradient of the above system is given by

$$\mathbf{A} = \begin{pmatrix} 2K_5 M & 6K_5 N - \delta \\ \delta - 2K_5 N & -2K_5 M \end{pmatrix}. \tag{13}$$

The dynamics of Eq. (12) will be investigated next as a function of the parameter $R = -\delta/\sqrt{12K_5 E_0} \geq 0$. It will be seen that the parameter R is useful in characterizing the phase trajectories of Eq. (12). Three cases, depending on the size R, will be examined.

Suppose that $R = 0$. This case corresponds to $\Delta = 0$, i.e. $f(X) = -\delta/K_0$, or when both $\delta = 0$ and $f(X) = 0$. Note that $K_0 \neq 0$, except when $\beta = 0$. Setting $dM/dX = 0$, $dN/dX = 0$, and $M = 0$, gives the two centers, at $(M, N) = (0, \pm\sqrt{E_0}/\sqrt{3K_5})$. They are centers since the eigenvalues of $\mathbf{A}$ are imaginary. Setting $N = 0$, $dM/dX = 0$ and $dN/dX = 0$, gives the radius of the bounding circle, at $\sqrt{E_0}/\sqrt{K_5}$, beyond which the orbits diverge. Additionally, there are two saddle points at $(M, N) = (\pm\sqrt{E_0}/\sqrt{K_5}, 0)$. These are saddle points since the eigenvalues of $\mathbf{A}$ are real, distinct, and of opposite sign. Motion along the limiting circle takes place in such a way that $\mathcal{A}_1 = 0$ and $\mathcal{A}_2 = E_0/\sqrt{K_5}$. If, for example, $\mathcal{A}_1 \neq 0$ and $\mathcal{A}_2 = 0$ initially, motion in the plane takes place along the line $N = 0$ up to the limiting curve, the phase Ω is then equal to $\pi/2$. From Eq. (9), it may be inferred that Ω in this limit is given by

$$\Omega_X - 2K_5 E_0^{1/2} \cos\Omega = 0. \tag{14}$$

The transition from $\sin\Omega = 1$ to $\sin\Omega = -1$ occurs along the limiting circle. The distance X on which this transition occurs is infinite, but it can be estimated by solving Eq. (14). The solution is

$$\Omega = \tan^{-1}[\exp(-2K_5 E_0^{1/2} X)\tan\Omega_0]$$

and hence, an estimate of the spatial length for which the energy of the first wave packet makes an almost complete transition to the second one is

$$L \approx 1/2K_5 E_0^{1/2}.$$

The distance in which this energetic exchange occurs is denoted subsequently as the "interaction length." The variation of the amplitude of A_2 along $N = 0$ may be discerned from

$$A_{2X} = K_5 A_2^2 - E_0, \tag{15}$$

which is obtained by eliminating P from Eq. (9) and making use of the energy relationship. The solution of Eq. (15) is

$$A_2 = (E_0/K_5)^{1/2} \tanh[K_5^{1/2} E_0^{1/2} (X - X_0)],$$

with $\mathcal{A}_2 = (E_0/K_5)^{1/2} \tanh[(K_5 E_0)^{1/2} X_0]$. At the beginning of the growth process, $A_1 \gg A_2$ so that $\sin\Omega = 1$ and the growth of the second mode is independent of $\mathcal{A}_2$. With the solution of A_2 in hand, using Eq. (10) and the first expression of Eq. (9), it can be shown that

$$A_1(X) = \frac{\mathcal{A}_1}{\sqrt{1 - \tanh^2[K_5^{1/2} E_0^{1/2} X_0]}} \operatorname{sech}\sqrt{K_5 E_0}(X - X_0).$$

This solution shows that irreversible energy conversion from A_1 to A_2 takes place for $R = 0$. This solution is not stable, however, since the stationary states are reached by motion along the limiting curve on the phase plane. The smallest variation of R away from zero invariably results in motion along homoclinic orbits with consequent oscillations in the amplitude of A_1 and A_2.

The dynamics when $R \neq 0$ but small are similar to the $R = 0$ case, and the phase trajectories are similar in structure. The phase plane depicted in Figure 2 corresponds to $R \neq 0$ but small. The phase portrait for $R = 0$ would be similar except that the lobes would be symmetric about the $N = 0$ axis.

In this case the phase is described by

$$\Omega_X + \delta - 2K_5 E_0^{1/2} \cos\Omega = 0. \tag{16}$$

Consequently, the interaction length, assuming δ is constant, decreases as δ increases:

$$L = \frac{1}{\sqrt{4K_5 E_0^{1/2} - \delta^2}}. \tag{17}$$

With regards to the sand ridge model, the interaction length is correlated to the inter-bar spacing. From the above expression it is seen that the bar spacing will decrease for higher frequencies of the water waves, and/or when the energy in the water wave spectra is reduced, and will also progressively decrease if the bottom topography is sloped.

For $R \ll 1$ the centers are at $(M, N) = (0, \frac{\delta}{6K_5}[1 \pm \sqrt{1 + \frac{12K_5 E_0}{\delta^2}}])$, and the line $N = 0$ is no longer the line of symmetry. Also, the line $N = \frac{\delta}{6K_5}$ will not generally intersect the limiting circle, as shown in Figure 2.

When $R \gg 1$, instead of a pair of stationary solutions, only one is possible, and the energy is concentrated mainly in the lower mode. The two modes interact weakly, and the spatial beats get smaller and shallower as the detuning paramenter is increased. The phase portrait for this case is shown in Figure 3. In this regime, $A_1(X)$ will have nearly constant amplitude, approximately equal to $\mathcal{A}_1$, and A_2 will show very shallow and frequent oscillations in its amplitude.

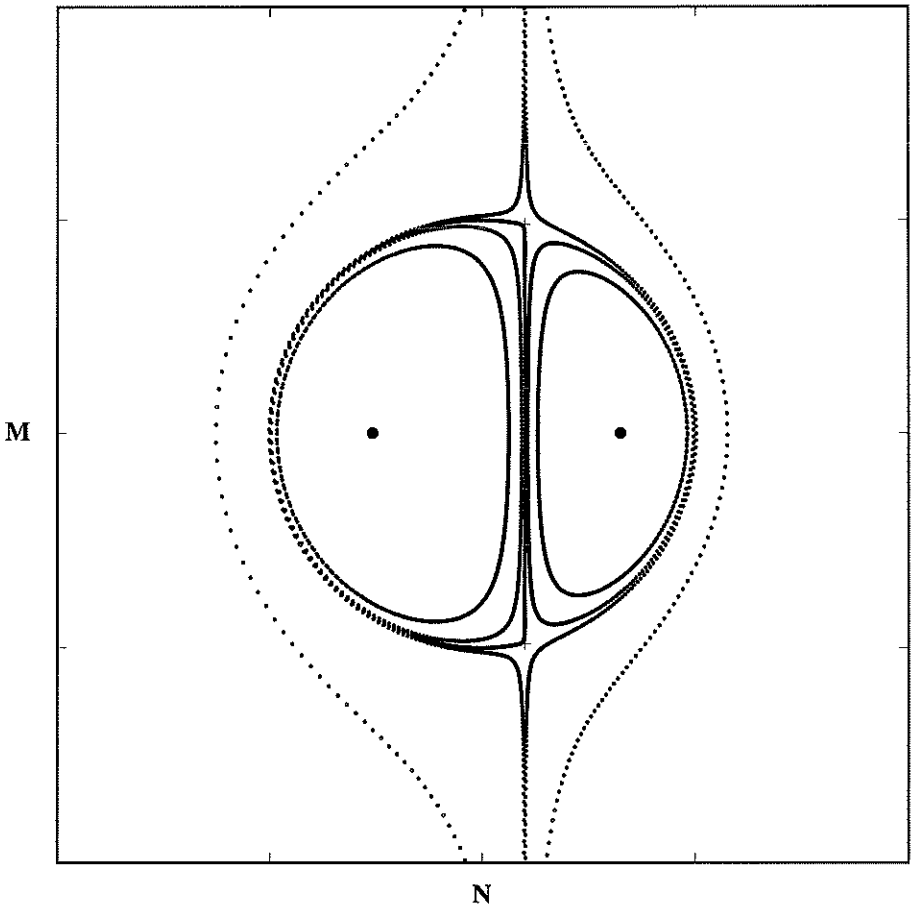

FIGURE 2. Phase plane of A_2 for $R \ll 1$, when $f(X, y) = 0$. The N axis increases to the right. The M axis is vertical. The dots indicate the location of the centers.

If dissipative effects were to be included in the model for the surface waves in the form of a Rayleigh-type dissipative mechanism, representing the combined effect of bottom drag and surface losses, and it is assumed that these affect both modes in the same way, then

$$\begin{aligned} A_{1X} - K_5 A_1 A_2 \sin\Omega + \chi A_1 &= 0 \\ A_{2X} + K_6 A_1^2 \sin\Omega + \chi A_2 &= 0, \end{aligned}$$

where χ is a positive real constant. The phase equation remains similar to its non-dissipative counterpart.

When dissipation is included, energy is no longer conserved. The wave packets are now constrained by

$$K_5(M^2 + N^2) + K_6 P = E_0 e^{-2\chi X},$$

and the dynamics of A_2 is given by

$$\frac{dM}{dN} = \frac{K_6^2 M^2 + (2K_5^2 + K_6^2)N^2 - K_5\chi M - K_5\Delta(X)N - K_6 E_0 e^{-2\chi X}}{K_5(\Delta(X) - 2K_5 N)M - K_5\chi N}.$$

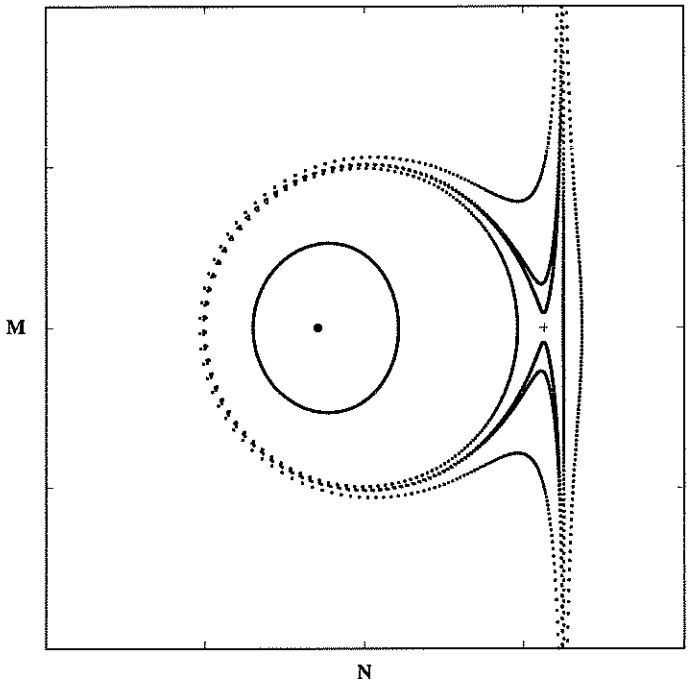

FIGURE 3. Phase plane for A_2 for $R \gg 1$. The dot indicates location of center, the cross indicates the location of saddle point.

Introducing the new variables

$$M = \tilde{M} E_0^{1/2} e^{-\chi X}$$
$$N = \tilde{N} E_0^{1/2} e^{-\chi X}$$

and the reduced distance

$$\xi = 2E_0^{1/2}(1 - e^{-\chi X})/\chi,$$

one obtains

$$\frac{d\tilde{M}}{d\tilde{N}} = \frac{K_6^2 \tilde{M}^2 + (2K_5^2 + K_6^2)\tilde{N}^2 - K_5 E_0^{-1/2}(1 - E_0^{-1/2}\chi\xi)\Delta(\xi)\tilde{N} - 1}{K_5 E_0^{-1/2}\Delta(\xi)(1 - E_0^{-1/2}\chi\xi)\tilde{M} - 2K_5^2 \tilde{M}\tilde{N}}. \tag{18}$$

Assuming $\Delta = 0$, the system phase trajectories are described by

$$\frac{2d\tilde{M}}{d\tilde{N}} = \frac{1 - K_6^2 \tilde{M}^2 - (2K_5^2 + K_6^2)\tilde{N}^2}{\tilde{M}\tilde{N}}$$

which has the same structure in the phase plane as the $R = 0$ non-dissipative case, with the important distinction being that ξ is related nonlinearly to X. Thus, the damping of the waves is characterized by

$$\tilde{\chi} = \chi/(2K_5 E_0^{1/2}).$$

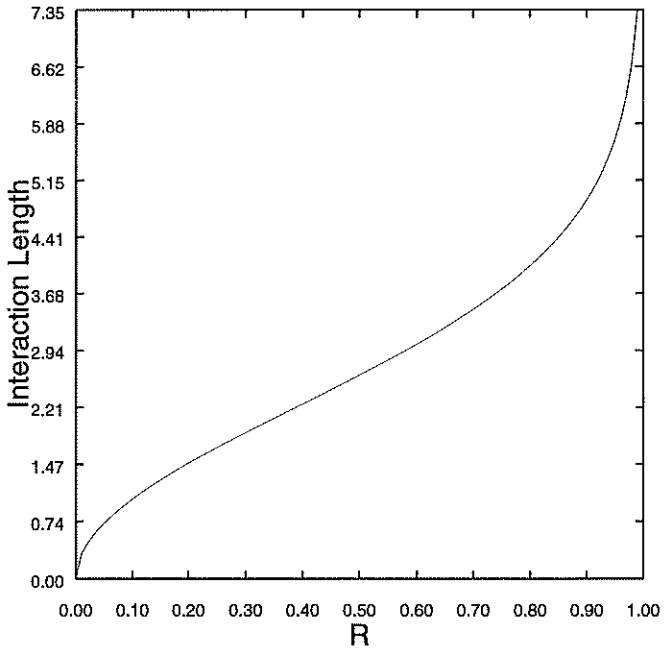

FIGURE 4. Interaction length dependence on the nonlinear parameter R. The detuning parameter is scaled so that as $\delta \to 0$, $R \to 1$.

For $\tilde{\chi} \ll 1$, there is weak damping, and the waves travel a considerable distance before the energy is fully dissipated. On the other hand, if $\tilde{\chi} \gg 1$, only a small arc of the trajectory in phase plane is traversed. The waves substantially attenuate over short distances.

In summary, the parameter R is useful in characterizing the behavior of the solutions of the wave packet system. Basically, there are two regimes in R. The solutions for small R are characterized by long interaction lengths and substantial sharing of the energy among the wave packet amplitudes. The wave packet amplitudes have an oscillatory behavior in X and nonlinear effects are more important. The form of the solutions is akin to Jacobi Elliptic functions. The interaction length is relatively insensitive to δ and substantial power transfer occurs, the interaction length is very large. For R large, the interaction length is fairly short and there is less energy interchange among the wave packet amplitudes. The amplitude of the first wave packet is nearly constant and the amplitude of the second wave packet oscillations is proportional to $1/\delta$. The second mode oscillates sinusoidally with a frequency proportional to $1/\delta$. Figure 4 summarizes how the interaction length varies nonlinearly over the range of R.

3. Steady Bottom Configurations of the Reduced Model

Numerical solutions to the full model were presented in [11]. They showed that initially smooth bottom topographies developed bar-like structures and that bar generation was a fairly smooth process in time. The bars developed refractive patterns in response to an uneven incoming wave spectra, or when there was a gradient in the initial bottom topography. Other phenomena, such as tuning between the bar features and the water waves, smooting

of features in the initially rough bottom topographies were also possible. As a general rule the water waves had a stronger effect in reshaping the bottom topography than the bottom had on the water waves. The process of readjusting of the water wave/bottom topography system lead at times to the displacement and transformation of the bottom, changes that persisted until some quasi-equilibrium configuration was reached. This quasi-equilibrium was such that the bars did not move appreciably in X and y, however, they did continue to grow in size.

Attention is now focused on finding steady solutions of the reduced model. For steady bottom configurations, $\partial h/\partial T = 0$, and Eq. (8) may be integrated. Such integration yields an integration constant Γ. It is then possible to write the bottom topography in terms of the wave packet amplitudes. After integrating, the bottom topography is given by

$$Ah^4 - Bh^2 + C = 0, \tag{19}$$

where

$$\begin{aligned} A =& c_1^2 w_1 + c_2^2 w_2 \\ B =& 2(c_1 w_1 + c_2 w_2) \\ C =& w_1 + w_2 - \Gamma \end{aligned}$$

and $c_i = \frac{1}{2}\beta^2 k_i^2$, with $i = 1, 2$. The functions w_i are

$$w_1 = M^2 + N^2$$

and

$$w_2 = \frac{E_0}{K_6} - \frac{K_5}{K_6} w_1.$$

Since the bottom must be positive, the relevant square root of Eq. (19) is

$$h^2 = \frac{B + [B^2 - 4AC]^{1/2}}{2A}, \tag{20}$$

and it determines physically-relevant configurations. Furthermore, since h^2 cannot be complex, there is a threshold condition for the constant of integration Γ. This condition will be examined shortly.

When the expression for f, in terms of M and N, is substituted into Eq. (11), it is then possible to examine the issue of steady bottom configurations since they are given by

$$\frac{dM}{dN} = \frac{K_5(M^2 + 3N^2) - [\delta + K_0 f(M,N)]N - E_0}{([\delta + K_0 f(M,N)] - 2K_5 N)M}. \tag{21}$$

The global behavior of the above system will be inferred by studying the behavior of the linearized version at specific points of the phase plane as well as by direct numerical integration. The gradient of Eq. (21) is given by

$$\begin{pmatrix} 2K_5 M - K_0 N \frac{\partial f}{\partial M} & 6K_5 N - \delta - K_0 \frac{\partial (fN)}{\partial N} \\ \delta - 2K_5 N + K_0 f + K_0 M \frac{\partial f}{\partial M} & -2K_5 M + K_0 M \frac{\partial f}{\partial N} \end{pmatrix}.$$

Comparison of the above expression with Eq. (13) suggests that the phase dynamics are very similar when f is a smooth function of M and N. As in the previous case, there is a limiting circle of axis length E_0/K_5. Beyond this circle conservation of energy is violated. Thus, all physically-relevant solutions lie within this limiting curve. When $M = 0$ and $dM/dX = 0$, the N coordinate of the critical points are given by the points of intersection of two curves $\Xi = 3K_5N^2 - \delta N - E_0$ and $K_0 f(0, N)N$, i.e. points where

$$\Xi = K_0 f(0, N)N. \tag{22}$$

The Ξ curve is always convex for physically-relevant conditions. The curve $K_0 f(0, N)$ is even for all N. This can be demonstrated algebraically by confirming that $K_0 f(0, N) - K_0 f(0, -N) = 0$. Hence the function $K_0 f(0, N)N$ is odd.

Since Eq. (22) is quadratic, it is natural to ask whether there are real roots, and if so, and whether there are two, or one. The roots of Eq. (22) are given by

$$\frac{\delta + K_0 f(0, N)}{6K_5} \pm \frac{1}{6K_5}\left([\delta + K_0 f(0, N)]^2 + 12K_5E_0\right).$$

It is immediately clear that since the discriminant is always positive, there will always be real roots and there will be two. However, only one root is relevant if the root is not bound by $|N| \leq \sqrt{E_0/K_5}$, since this is the radius of the bounding circle. Moreover, if $[\delta + K_0 f(0, N)]^2 \gg 12K_5E_0$, the problem will be dominated by the single root at approximately $\frac{\delta + K_0 f(0,N)}{6K_5}$. Hence, the appearance of the bottom topography in the above expression would require us to redefine the parameter R. The new definition would be $R = [\delta + |K_0\tilde{f}|]/(12K_5E_0)^{1/2}$, where $\tilde{f} = f(0, N)$. Doing so would require an estimate of the size of $K_0\tilde{f}$. In what follows, however, the old definition of R is retained.

Whether these critical points are centers, saddles, or spirals is determined by solving for λ in

$$\lambda^2 = (6K_5N - \delta - K_0\frac{\partial(N\tilde{f})}{\partial N})(\delta - 2K_5N + K_0\tilde{f}). \tag{23}$$

If the value of λ^2 is negative these critical points are centers. The absence of the term $K_0N\frac{\partial\tilde{f}}{\partial M}\lambda$ in the above equation results from the fact that the term vanishes. This can be shown by direct calculation. In order to determine the nature of the critical points, the solutions to Eq. (23) will be investigated, using values of N given by solutions to Eq. (22).

To do so, we first need to determine a sensible value for the parameter Γ, such that h^2 is non-negative. The gridded areas of Figure 5 give the range of Γ, for a sufficiently large span of N, for which the discriminant in Eq. (20) is non-negative.

By fixing the energy $E_0 = 1$, and $\Gamma = 1$, a direct calculation shows that with $\omega = 1.2$, λ^2 is indeed negative for a range of β and N as shown in Figure 6a. On the other hand, if $\beta = 0.08$, fixed, and vary ω and N, Figure 6b shows a range for which λ^2 is negative. The numerical values of the parameters are chosen to be fairly representative of the geophysical context. These calculations show that the critical points, which lie on the $M = 0$ axis, are centers in the range $-0.5 \geq N \geq 0.5$ for the choice of parameters chosen. As will be

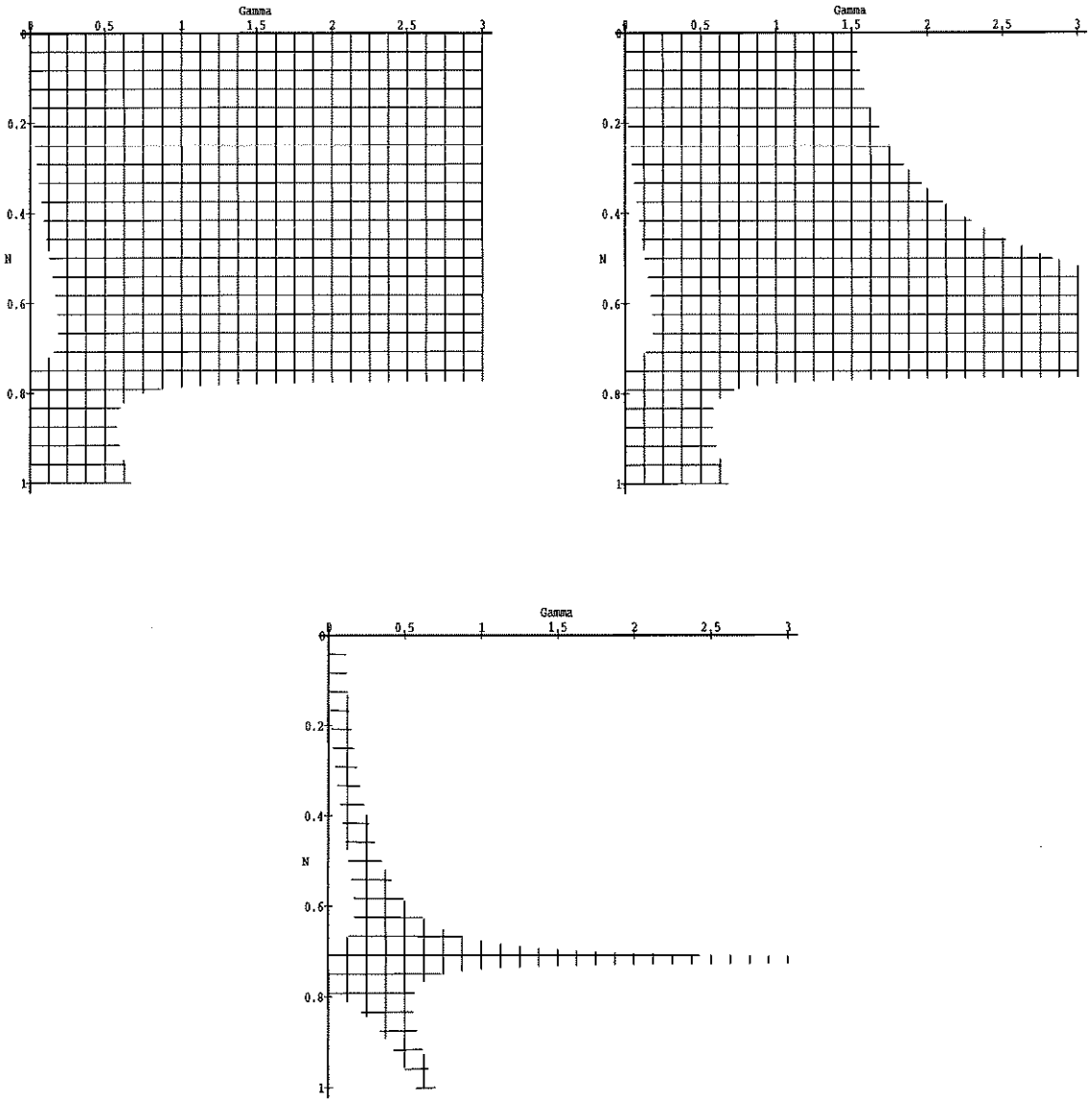

FIGURE 5. Shaded area corresponds to values of Γ that makes the discriminant in Eq. (20) non-negative. In order of increasing β and R. (a) $\beta = 0.06$, $R = 0.021$, (b) $\beta = 0.12$, $R = 0.085$, and (c), $\beta = 0.24$, $R = 0.411$.

shown momentarily, this range of N is sufficient to cover the numerical cases that have been chosen for illustration.

Figure 7a, b, and c, show how the curves $K_0 \tilde{f} N$ and Ξ change with increasing R. The curves were computed having fixed $\omega_1 = 1.2$, $E_0 = 1$, and $\Gamma = 1$. Figure 7a corresponds to $\beta = 0.06$ and $R = 0.021$. Figure 7b corresponds to $\beta = 0.12$ and $R = 0.085$, and Figure 7c to $\beta = 0.24$ and $R = 0.411$, which shows only one intersection between the curves. In

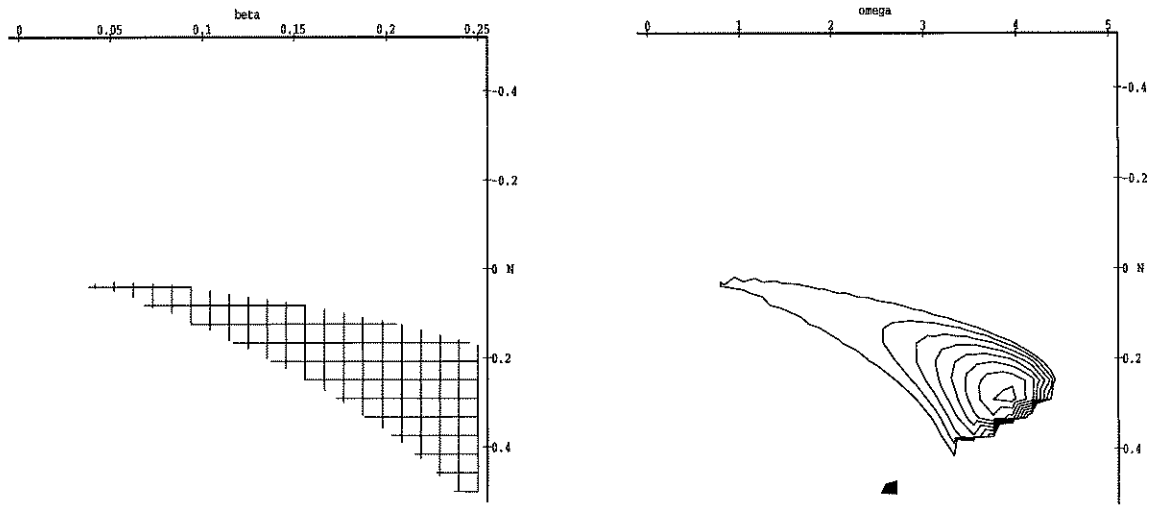

FIGURE 6. $\lambda^2 < 0$ graph, with $E_0 = 1$, $\Gamma = 1$. (a) As a function of N and β, with $\omega_1 = 1.2$ fixed. (b) as a function of N and ω, with $\beta = 0.08$ fixed.

all cases, the intersections fall in the range $-0.5 \geq N \geq 0.5$. As R increases, the minima of the curve moves in the positive N direction, hence the centers move in the positive N direction with increasing R. The Ξ curve is convex, with a minimum value $-E_0 - \delta^2/12K_5$, which happens when $N^\star \equiv \delta/6K_5$, whereas $K_0 N \tilde{f}$ is odd. The effect of decreasing the value of Γ/E_0 places the centers further appart. If the value of R is small, the Ξ curve will have a small value below zero, and $K_0 f(0, N)$ will be a fairly shallow curve that will then decrease very rapidly when N is large.

To illustrate Eq. (21) and to demonstrate qualitatively that the parameter R remains useful in characterizing the solutions to the equation the dynamical system was inserted into the numerical code dstool [8]. All phase plane figures in this study were produced with dstool. When $R \ll 1$, which corresponds more closely to the oceanic situation in which bars presumably occur, the centers are given by the intersection of the curves $K_0 \tilde{f} N$ and Ξ. The phase plane is quite similar to the case with a fixed bottom topography $f = 0$, which was discussed in the previous section. When $f(X, T)$ is fixed in time and equal to zero, there are always two centers and two saddle points for $R \ll 1$. However, when the bottom is allowed to adjust to its steady form, the bottom topography is never flat and the nature of the critical points may be different from the fixed bottom case. The bar morphology in this case will depend most crucially on how the curves $K_0 \tilde{f} N$ and Ξ intersect as well as the data at $X = 0$, the latter determining which orbit in phase space the system will take.

For the smaller R cases, the area of phase space occupied by solutions of one phase or the other are nearly equal. As R increases, more combinations of initial conditions, which fix the orbits, are likely to have the phase of the left-most center, i.e. the center with negative N coordinate. Qualitatively, bedforms that are the result of data which trace orbits that visit the neighborhood of the saddle points have steep troughs and smooth peaks or vice versa, depending on which center the orbits trace. If the data chooses orbits

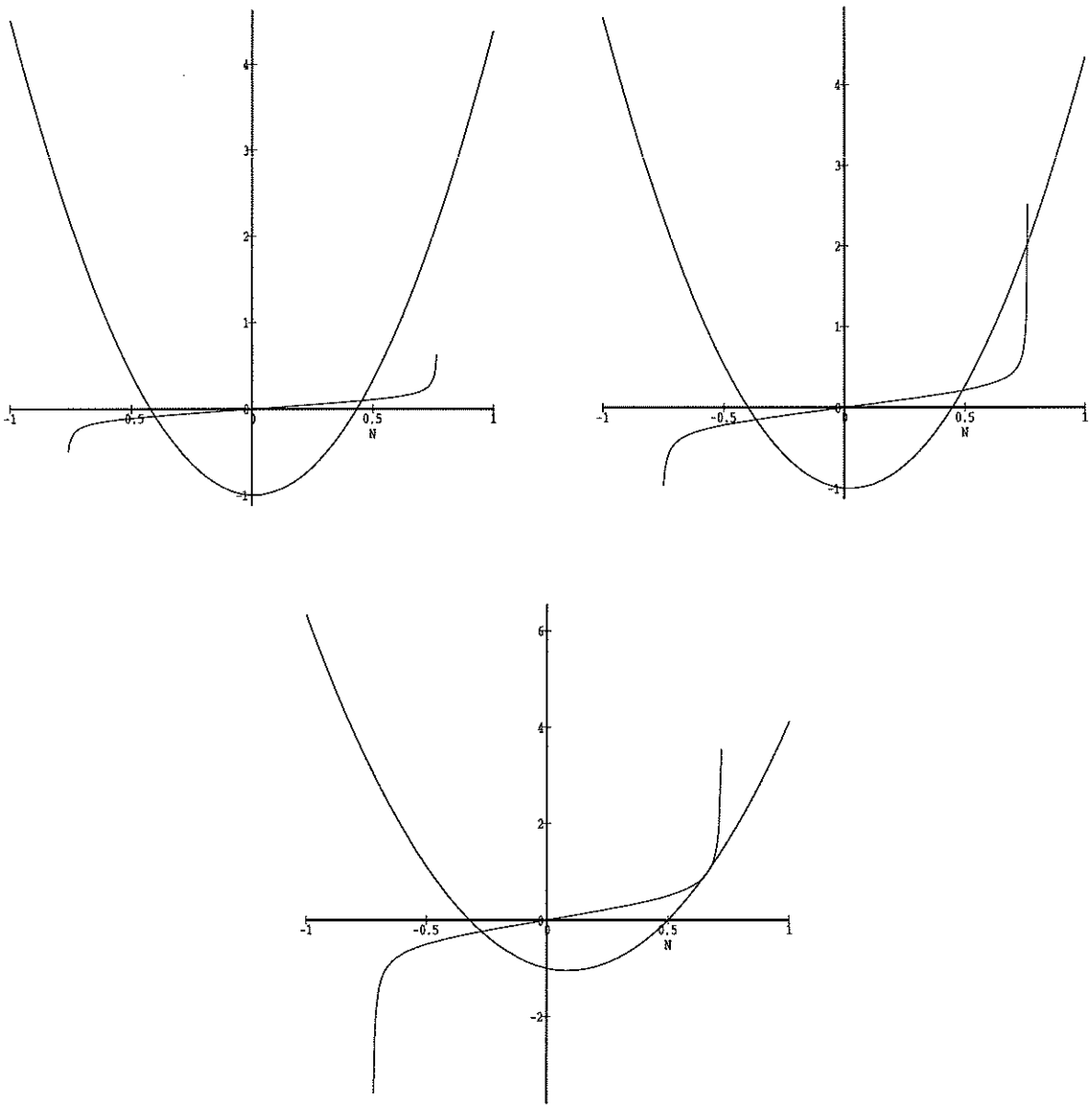

FIGURE 7. Eq. (22) with increasing β and R. Ξ is the even and convex curve and $K_0\tilde{f}N$ is the odd curve. The intersections of the 2 curves give the location of the centers. In all plots $\omega_1 = 1.2$, $E_0 = 1$, and $\Gamma = 1$. (a) $\beta = 0.06$, $R = 0.021$, (b) $\beta = 0.12$, $R = 0.085$, and (c), $\beta = 0.24$, $R = 0.411$.

that are always close to the centers the outcome will be bars that are nearly sinusoidal in shape. When only a one center predominates, as is the case with the $R = 0411$ case, the orbits share the same phase and are structurally more similar to each other. The steady topographies, plotted as functions of X, with $E_0 = 1$, $\omega_1 = 1.2$, and $\Gamma = 1$ are shown in Figure 9. They correspond to the phase portraits of Figure 8. The horizontal length scale

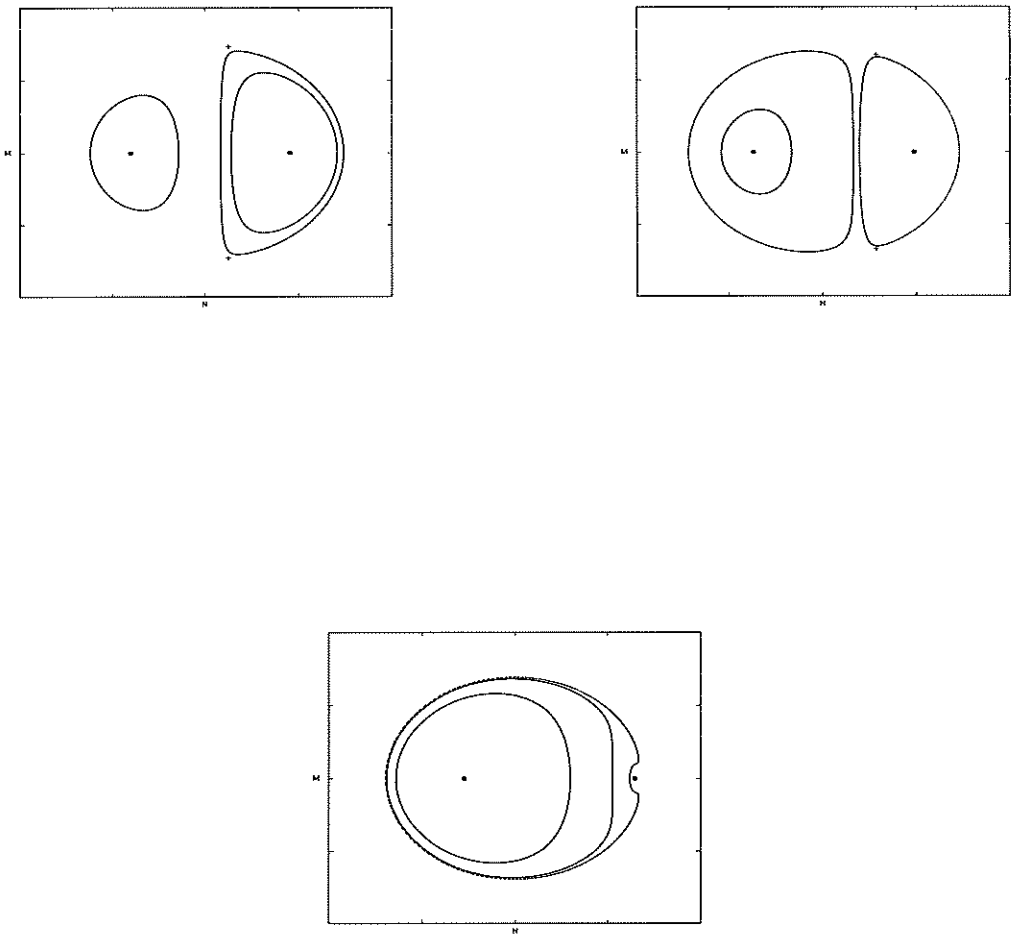

FIGURE 8. Solutions of Eq. (19) with $E_0 = 1$, $\omega_1 = 1.2$, $\Gamma = 1$. N increases to the right. The centers are indicated by dots and the saddle points by crosses. In order of increasing R: (a) $\beta = 0.06$, $S = 41.67$, $R = 0.021$; (b) $\beta = 0.12$, $S = 10.42$, $R = 0.085$; (c) $\beta = 0.24$, $S = 2.4$, $R = 0.411$.

is arbitrary but the same in all plots. The amplitude of the bars is arbitrary and relative only to each graph. The initial data, that is (N, M) at $X = 0$, not only chooses an orbit to follow, an orbit which is homoclinic for all physically-relevant stable situations, but it also determines the horizontal mean "height" of the function f, representing the bottom topography. The graphs are arranged in order of increasing R. Figure 9a, corresponds

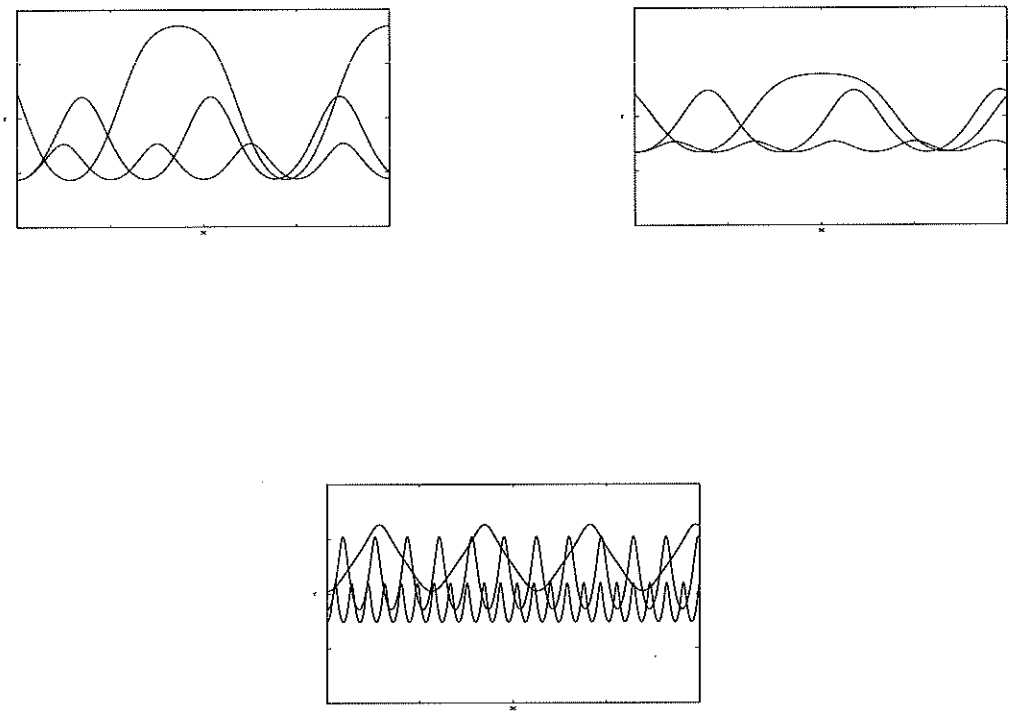

FIGURE 9. Steady bedforms, given by the orbits in Figure 8. With $E_0 = 1$, $\omega_1 = 1.2$, and $\Gamma = 1$, fixed. The horizontal length scale is arbitrary but the same in all plots. The amplitude is arbitrary and relative to each graph. Clockwise, in order of increasing R: (a) $\beta = 0.06$, $S = 41.67$, $R = 0.021$. The largest bars are the result of orbits with data (N, M) at $X = 0$, $(M, N) = (0.142, 0.695)$; the next largest bars result from data $(0.0, 0.142)$, the smallest bars correspond to $(0.0, -0.142)$. (b) $\beta = 0.12$, $S = 10.42$, $R = 0.085$. The largest bars correspond to $(0.299, 0.651)$. Next in size, are bars generated with $(0.164, 0.0)$; the smallest with data $(-0.1640.0)$. (c) $\beta = 0.24$, $S = 2.4$, $R = 0.411$; the largest bars correspond to $(0.619, 0.0)$, the next two correspond to $(0.525, 0.0)$ and $(0.299, 0.0)$, respectively.

to $\beta = 0.06$. The computed Stokes number for this case is $S = 41.67$, and $R = 0.021$. The largest bar structure in the figure corresponds to the orbit in Figure 8a that circles the right center and that visits the neighborhood of the saddle points. The topography is characterized by sharp troughs and long peaks. The next largest stable bar configuration in Figure 9a corresponds to an orbit around the right center and it shows sharp peaks and shoother troughs. The smallest bar configuration corresponds to an orbit around the

left center with small data. The orbits produce smoother and more symmetric bars, the closer the data is to a center and farther away from the saddle points. Figure 9b shows the stable bars for the $\beta = 0.12$, $S = 10.42$, and $R = 0.085$ case. The largest steady bars correspond to an orbit near that visits the neighborhood of the saddle points and encircles the right center. The trough to peak assymetry is more pronounced. Next in size are the bars generated by a trajectory that orbits the left center, which has sharp peaks and smooth toughs; the smallest bars correspond to a trajectory that orbits the left center critical point. Figure 9c corresponds to the $\beta = 0.24$, $S = 2.4$, and $R = 0.411$ case. The largest bars and most unusual bars correspond to the largest trajectory in Figure 8c. The next two correspond to orbits in Figure 8c that have smaller trajectories. Figure 8c shows most clearly that the amplitude of the bars and their interbar spacing are not in direct proportion to each other. This is characteristic of the predictions of this model. The bars in this case are more apt to have a more sinusoidal profile.

When $R \gg 1$, instead of a pair of stationary solutions, only one is possible, and the energy is concentrated mainly in the lower mode. The two wave packets interact weakly, and the spatial beats get smaller and shallower, as the detuning paramenter is increased, or the energy in the data is decreased. The topology of the phase plane orbits for high R is very similar if f is fixed in time and constant to the case when bedform is included in the dynamics, provided the bedform has the same bias. Prior to considering the steady bedform issue, it is instructive to examine the behavior of the wave packets, as they propagate over a temporally-fixed, constant topography as well as over a sloped bottom topography. In the $R \gg 1$ regime, $|A_1|^2 \approx |\mathcal{A}_1|^2$. Suppose, for simplicity, that $A_2(0) \sim 0$. Then the last expression of Eq. (9) may be integrated so that the phase would be, approximately,

$$\Omega = -\delta X + K_0 F(X) + \frac{\pi}{2}, \tag{24}$$

where $F(X) = \int^X f(s)ds$, having assumed that $f(0) = 0$. Substituting Eq. (24) into Eq. (9), one can show that

$$A_2 = \mathcal{A}_2 + K_6|\mathcal{A}_1|^2 \int^X \cos(\delta s - K_0 F(s))ds.$$

Supposing that $f(X) = -\nu$, where ν is a positive constant,

$$A_2 = \mathcal{A}_2 + \frac{K_6}{\delta + K_0\nu}|\mathcal{A}_1|^2 \sin(\delta + K_0\nu)X.$$

Hence, the wave packets vary sinusoidally in X, with a repetition length $L \approx \pi/(K_0\nu + \delta)$, which is inversely proportional to the detuning parameter and to the bottom topography bias ν. The above expression suggests that the dynamics of the water waves depend crucially on the depth of the water column. Moreover reasonable answers are obtained only if the basic assumption about the size of the fluctuations of the bottom topography is enforced. If the bottom is gently sloping, $f(X) = -\nu X$, then

$$A_2 = \mathcal{A}_2 + \frac{K_6\sqrt{\pi}}{\sqrt{K_0\nu}}|\mathcal{A}_1|^2 \left[\cos(\frac{\delta^2}{2K_0\nu})\mathrm{C}(z) - \sin(\frac{\delta^2}{2K_0\nu})\mathrm{S}(z)\right],$$

where

$$z = \sqrt{\frac{1}{2K_0\pi\nu}}(\delta + K_0\nu X)$$

and C and S are the Fresnel integral functions. Hence, as the waves shoal over a sloped bottom, the water waves will have a decreasing interaction length and less of the energy will be shared among the fundamental wave packet and its first harmonic wave-packet.

Returning to the issue of steady bottom configurations, the constraint on the bottom reads approximately

$$(1 - c_1 h^2)|\mathcal{A}_1|^2 + (1 - c_2 h^2)|A_2|^2| = \Gamma,$$

for $R \gg 1$. Without solving explicitly for the bottom topography, it is seen from the above expression that the steady bottom configurations are very mildly sinusoidal with zero mean slope. The waviness is imparted by the influence of the second wave packet oscillations and the bottom reacts very mildly to the water waves.

In conclusion, the stable bottom configurations predicted by this model are periodic and have a zero mean slope. Initially-sloped bedforms develop bars with increasing inter-bar spacing and amplitude, as the distance from the shore increases. Furthermore, the bed tends to adjust to a zero average slope, particularly in shallow waters. Increasing the total energy E_0, holding other parameters constant, will decrease R and hence the water wave packets will share more equally the available energy. The result is that the bottom topography has the potential of being very far from sinusoidal in appearance, particularly, if the solution has initial data which generates a homoclinic orbit that traverses the neighborhood of the saddle points.

The other key morphological features of bars are their height and their spacing. Height is unfortunately beyond our analysis of stable bedform configuration, since there is a free parameter Γ, which affects the height predictions in a very crucial way. However, it is possible to make an assessment of the relative importance of dispersive versus nonlinear effects in controlling the inter-bar spacing. With repeated experimentation, data was collected that shows the dependence of the interaction length for the resulting steady bars on the parameters that determine the water waves.

Figure 11 illustrates the dependence of the interaction length, normalized by the wavelength of the fundamental frequency, on the nonlinear parameter α and the dispersion parameter β in the regime $R < 1$. An estimate of the size of the parameters α and β in the geophysical context is, $\alpha < 0.15$, and $0.005 < \beta < 0.20$. Not surprisingly, dispersive effects play a more important role in the determination of the interbar spacing than the nonlinearity of the water waves, especially for higher frequencies. Nevertheless, nonlinear effects participate in the determination of the inter bar spacing in ways that are significant: when both parameters are large, as is evident in the graphs, the interaction length are unlike any predictions derived from linear theory.

To conclude this section, we consider two interrelated question relevant to the dynamics of the bedforms: to determine the direction in which bars tend to move, and secondly, to determine why some of the time-dependent solutions reported in [14] exhibit little or no stabilizing trend in bar amplitude. In terms of the reduced model, these questions translate into finding whether sediment fluxes are shoreward or seaward, as given by Eq (7) and (8).

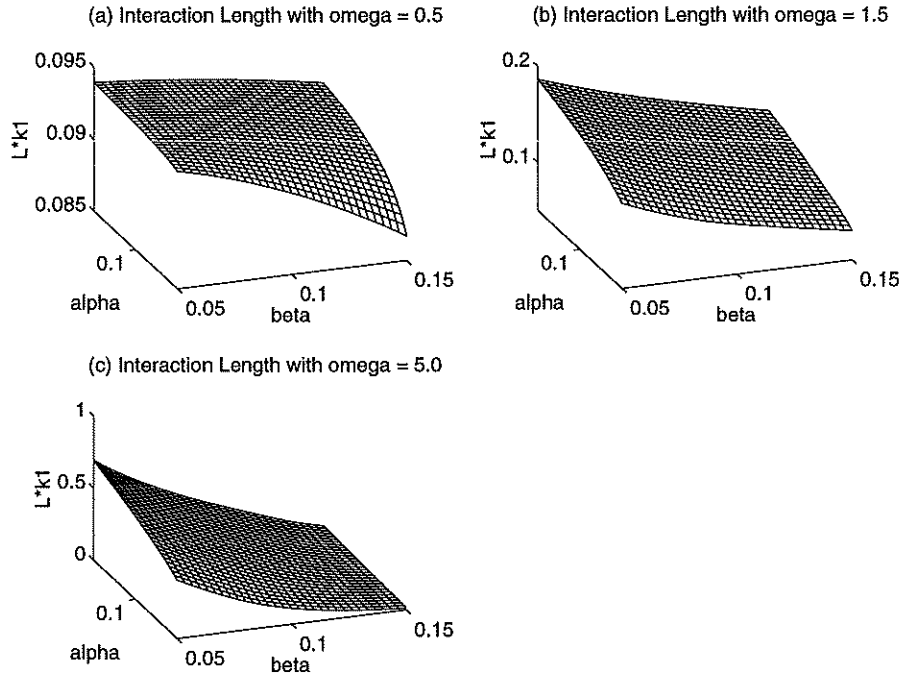

FIGURE 10. Interaction length L dependence on α and β for different frequencies, with $R < 1$. The interaction length is normalized by the wavenumber of the fundamental, k_1. (a) $\omega_1 = 0.5$, (b) $\omega_1 = 1.5$, (c) $\omega_1 = 5.0$.

First, Eq (8) is recast as

$$\left(\frac{K}{\rho_0}\right)^{-1} \frac{\partial h}{\partial T} = \frac{\partial U}{\partial h}\frac{\partial h}{\partial X} + \sum_{i=1}^{2} \frac{\partial U}{\partial a_i}\frac{\partial a_i}{\partial X} + \sum_{i=1}^{2} \frac{\partial U}{\partial a_i^*}\frac{\partial a_i^*}{\partial X},$$

assuming that U is smooth enough to permit differentiation. The quantitity $\frac{K}{\rho_0}$ is set to unity in what follows, since this constant just scales T. Some headway can be made by computing explicitly the terms in the above equation. The equation may be recast as

$$\begin{aligned}\frac{\partial f}{\partial T} = &-\frac{2\beta^2}{K_6}\{k_1^2 E_0 + (k_2^2 K_6 - k_1^2 K_5)(M^2 + N^2)\}(1+f)\frac{\partial f}{\partial X} \\ &-(K_6 - K_5) - \beta^2(1+2f)(k_1^2 K_5 - k_2^2 K_6),\end{aligned} \tag{25}$$

The term in front of $\partial f/\partial X$, which will be denoted v, is the speed at which the disturbance $\mathcal{F}(X - vT)$ in the initial bedform $\mathcal{F}(X)$ propagates. The speed v is approximately

$$v \approx \frac{2\beta^2}{K_6}\{k_1^2 E_0 - Q(M^2 + N^2)\},$$

where $Q = k_1^2 K_5 - k_2^2 K_6$. Evaluation of the expression in curly brackets shows that the speed is positive. Hence it can be concluded that the disturbance will travel primarily

towards the shore. That is, sediment will flux primarily in the shoreward direction, and its speed will increase quadratically with the dispersiveness of the waves and linearly with the energy in the wave. Since the quantity v oscillates between $\frac{2\beta^2}{K_6}\{k_1^2 E_0 - Q(M^2+N^2)\}$ and $\frac{2\beta^2}{K_6}\{k_1^2 E_0 - QS^2\}$, where S^2 is the smallest value attained by either N^2 or M^2, for any X, the characteristics emanating from the solution will focus and spread, as time goes on, making the flux oscillate mildly. Moreover, fluxes may attain a shocklike structure, if T is large enough.

The foregoing discussion, however, does not convey the whole picture on the evolution of the bottom topography, as given by the model. This is because the bottom topography is the result of solving the time-dependent model by the iterative procedure summarized in the introduction. It can be recast algorithmically as

$$\begin{aligned} 0 &= G(f_n, a_1^{n+1}, a_2^{n+1}) \\ f_{n+1} &= f_n + \Delta T \frac{\partial U(f_n, a_1^{n+1}, a_2^{n+1})}{\partial X} \\ f_0 &= \mathcal{F}(X), \end{aligned}$$

where $T = n\Delta T$ is the long-time variable, $n = 0, 1, 2, \ldots, n_f$. Posed this way, it is certainly possible that either this iterative procedure may diverge, unless certain fixed point conditions are met, or at the very least, produce answers that depend on ΔT. That is, it is possible that the model for the mass transport equation is not consistent with our expectations, or that the model fails even for in a single iteration. To investigate these possibilities, the mass transport equation is examined over a single ΔT interval of the iterative process.

First, the current bottom topography is expanded as

$$f = \epsilon^1 f_1 + \epsilon^2 f_1 + \ldots,$$

where $\epsilon \ll 1$, that is, a very gently sloping bottom. This expression is then substituted into Eq. (26). After collecting terms to lowest order,

$$\begin{aligned} \epsilon^1 : \quad & \frac{\partial f_1}{\partial T} + \frac{2\beta^2 Q}{K_6}\frac{\partial f_1}{\partial X} + 2\beta^2 Q_2 f_1 = Q_1 - \beta^2 Q_2 \\ \epsilon^2 : \quad & \frac{\partial f_2}{\partial T} + \frac{2\beta^2 Q}{K_6}\frac{\partial f_2}{\partial X} + 2\beta^2 Q_2 f_2 = -\frac{2\beta^2 Q}{K_6} f_1 \frac{\partial f_1}{\partial X} \end{aligned}$$

where $Q_1 = K_5 - K_6$, and $Q_2 = k_1^2 K_5 - k_2^2 K_6$. The solution to the lowest order equation is

$$f_1 = \frac{Q_1 - \beta^2 Q_2}{2\beta^2 Q_2}\left(1 - e^{-2\beta^2 Q_2 T}\right) + \mathcal{F}(X - \frac{2\beta^2 Q}{K_6} T) e^{-2\beta^2 Q_2 T}.$$

It is then possible to assertain the direction and rate of propagation of the the bottom from the above expression. It shows that the flux travels shoreward and that it has patches of converging sediment flux. However, since the argument in front of T in the exponents above

are small but negative, it means that the model predictions are sensitive to the iteration time step ΔT. From the modeling standpoint, this is a troubling issue, since it says that even in its simplest guize, the mass transport must include a dissipative mechanism. This is not an unsurmountable problem, since it is likely that the actual physical process is dissipative in nature anyway. In the numerical solution of the model [12], a dissipative numerical scheme was purposely used to solve the mass transport equation. This dissipative mechanism was sufficient to counteract the sensitivity of the solutions to the size of the time step, and hence made the solutions less sensitive to the size of the time step. For low resolution studies, this worked adequately, however, when the resolution was increased, the sensitivity of the solutions to the discretization became a problem. In the future, this issue will be revisited and a loss mechanism will be incorporated in newer versions of the model. To summarize, then, the fluxes tend to have a net shoreward direction in the reduced model. Secondly, the model requires the inclusion of a dissipative mechanism in the mass transport equation that would more properly convey the process of slow and smooth buildup of sedimentary structures by a two-time process. The inclusion of dissipation in the mass transport model would be best accompanied by the inclusion of losses in the surface wave model due to drag forces. The wave packet equations would then look similar to Eq. (18).

4. Conclusions

The most important finding from this study on the dynamics of a model for the formation and evolution of sand ridges on the continental shelf is that steady bottom configurations have the following characteristics: zero mean slope, smooth features, and are spatially periodic. Hence, if this crude model is a fair representation of the actual geophysical setting, in which the mean slope of the continental shelf over distances of tens of wavelengths, is very seldomly zero, it must be said that most sandbar configurations are non-steady and hence prone to move or change over time. In particular, initially-sloped bedforms develop bars with increasing interbar spacing and amplitude, as the distance from shore increases. Furthermore, the bed tends to be driven to zero mean slope conditions, particularly in shallow waters. The periodic nature of the bars is a direct result of the structure inherent in the nonlinear interaction of the wave packets that represent the water waves, which exchange energy in a repeating pattern. The distance over which these energetic exchanges occur is called the interaction length. The interaction length depends in a non-trivial way on the frequency of the water waves, as well as their energy, their nonlinearity and dispersiveness.

The stable bars can be broadly classified qualitatively in shape and in their capacity to interact with the water wave field, by the size of the parameter $R \equiv -\tilde{\delta}/\sqrt{12K_5E_0}\alpha$, which is the ratio of the detuning parameter (a negative quantity) to the square root of the energy of the wave packets E_0 times the nonlinear dimensionless parameter α. When R is small the wave packets will resemble Jacobi elliptic functions in shape, whereas when R is very large, they will resemble sinusoidal functions. The bars will then be functions of elliptic and sinusoidal functions, respectively. When R is small, which corresponds more closely to the geophysical setting in which bars occur, the ocean surface and the underlying topography will interact strongly, leading to more significant temporal adjustments of both

of these bodies. This is not the case when R is large, wherein the ocean and the bottom interact weakly.

Dispersive effects in the water waves tend to be more important than nonlinear effects in determining the spacing of the bars. Dispersive effects are also significant in determining the rate at which bars move on the bottom of the ocean. Since the reflected component of the water wave field was absent in this presentation, it is not surprising that the drift velocity generated by wave action was directed shoreward, in the direction of the incident waves.

The above conclusions regarding the sand ridge model apply only to a system with no spanwise dependence, yet the model which originally inspired this study is fully three-dimensional [14], and presumably capable of more interesting stable solutions. The key to understanding the full model is to have a good grasp of the solutions of Eq. (5). A separate study is underway to study this system of equations, which has fairly rich mathematical structure [10], and some relevance to nonlinear optics [15]. Nevertheless, the above findings are still valuable in interpreting the results of the full model and also serve as a check to the general behavior of the full model when the waves are nearly normal to the beach. In particular, this study suggests that the mass transport model should incorporate a dissipative mechanism, if the basic assumption on the smooth and slow buildup of sediment structures is to be retained in the theory.

Perhaps the three most interesting questions to be addressed at some point in the future are: (1) to investigate whether our educated guess on the relative unimportance of the boundary layer dynamics in the process of sand ridge generation in waters deeper than the break zone is really valid; (2) to investigate how the present models' results are affected by the incorporation of current-induced sediment motion; (3) to determine if the process of sand ridge motion is really controlled almost entirely by meteorological forcing, rather than by possible instabilities in the flow, as seems to be the case in sedimentary processes such as vortex ripple and cusp ripple formation. Preliminary numerical results which address the first question are encouraging. Currents in the ocean are important agents of motion for the sediment in the boundary layer. The present model is unable to take into account current effects, nevertheless, these would necessarily need to be accounted for when comparing model results to geophysical data. Incorporating current-driven effects into the model is not a simple process. However, Grant and Madsen [7] provide the framework. They suggest that the boundary layer of the bottom of the ocean be divided into a usually thinner wave-dominated boundary layer, hugging the bottom, and a larger current-dominated boundary layer. The second and third questions seem best answered by direct observation. However, the difficulties encountered in making such observations means that modeling and computing continue to be viable techniques in the pursuit of knowledge on this question.

APPENDIX

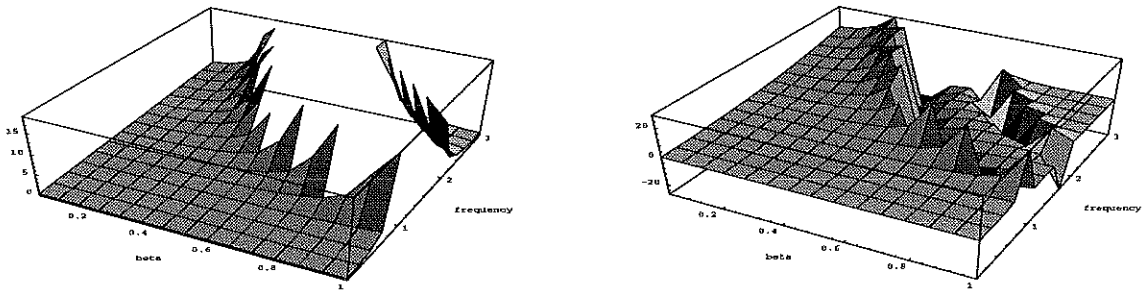

FIGURE 11. (a) Plot of K_5 versus the fundamental frequency ω_1, and β for the water wave problem. (b) Plot of K_6 versus the fundamental frequency ω_1, and β for the water wave problem.

The following are constants associated with Eq. (5):

$$K_1 = F_1$$
$$K_2 = F_2$$
$$K_3 = D_1 E_1$$
$$K_4 = D_2 E_2$$
$$K_5 = D_1 S_1$$
$$K_6 = D_2 S_2$$

with

$$D_j = [2(1 - \beta^2 \frac{\omega_j^2}{3})]^{-1}$$
$$E_j = k_j(1 - \frac{2}{3}\beta^2\omega_j^2)$$
$$F_j = 1/2k_j$$
$$S_1 = \frac{k_2 - k_1}{\omega_1}\{k_2 - k_1 + \omega_1(\frac{\omega_1}{k_1} + \frac{\omega_2}{k_2})\}$$
$$S_2 = \frac{2}{\omega_2}(k_1^2 + 2\omega_1^2).$$

The constants K_5 and K_6 are illustrated in Figures 11a and 11b, respectively. Note that D_j can become singular at $\omega_j = \sqrt{3}/\beta$. However, for small values of β, corresponding to the oceanic situation, this frequency is not reached under normal circumstances without violating the underlying model assumptions.

References

[1] M. J. Ablowitz & H. Segur, in *Solitons and the Inverse Scattering Transform*, Society for Industrial and Applied Mathematics, Philadelphia, PA, 1981.

[2] J. A. Armstrong, J. Ducuing & P. S. Persham, "Interaction between Light Waves in a Nonlinear Dielectric," *Physical Review* 127 (1962), 1918–1939.

[3] B. Boczar-Karakiewicz & R. G. D. Davidson-Arnott, "Nearshore bar formation by nonlinear processes," *Marine Geology* 77 (1987), 287–304.

[4] B. Boczar-Karakiewicz, D. L. Forbes & G. Drapeau, "Formation and stability of nearshore bars in the southern Gulf of St. Lawrence," *Geological Survey of Canada, Contribution 33187* (1990).

[5] P. Chossat & F. Dias, "The 1:2 resonance with O(2) symmetry and its applications to hydrodynamics ," *J. Nonlinear Science* 5 (1995), 105–129.

[6] M. H. Freilich & R. T. Guza, "Nonlinear Effects on Shoaling Surface Gravity Waves ," *Philosophical Transactions of the Royal Society of London* 311 (1984), 1–41.

[7] W. D. Grant & O. S. Madsen, "Combined wave and current interaction with a rough bottom," *J. Geophys. Res.* 84 (1979), 1797–1808.

[8] J. Guckenheimer, M. R. Myers, F. J. Wicklin & P. A. Wolfolk, "dstool: A Dynamical System Toolkit ," Center for Applied Mathematics, Cornell University, 1991.

[9] M. S. Longuett-Higgins, "Mass Transport in Water Waves," *Phil. Trans. Royal Soc. London* 245 (1953), 535–581.

[10] J. M. Restrepo, "A Model for the Formation and Evolution of Three-dimensional Sedimentary Structures on the Continental Shelf," Ph.D. thesis, The Pennsylvania State University, 1992.

[11] J. M. Restrepo & J. P. Albert, "Stability of simulton solutions of the equations for waves in quadratic nonlinear media," preprint, 1997.

[12] J. M. Restrepo & J. L. Bona, "Discretization of a Model for the Formation of Longshore Sand Ridges," *Journal of Computational Physics* 122 (1995).

[13] _____, "Model for the Formation of Longshore Sand Ridges on the Continental Shelf: The Interaction of Internal Waves and the Bottom Topography," Mathematics and Computer Science Division, Argonne National Laboratory, Report # MCS-P407-1293, December 1993.

[14] J. M. Restrepo, J. L. Bona, "Model for the Formation of Longshore Sand Ridges on the Continental Shelf," *Nonlinearity* 8 (1995), 781–820.

[15] M. J. Werner & P. D. Drummond, "Simulton solutions for the parametric amplifier," *J. Optical Society of America* 10 (1993), 2390–2393.

[16] G. B. Whitham, *Linear and Nonlinear Waves*, Wiley Interscience, New York, 1974.